ADVANCED SCIENCE Open Access
www.advancedscience.com

A Ternary Dumbbell Structure with Spatially Separated Catalytic Sites for Photocatalytic Overall Water Splitting

*Bocheng Qiu, Lejuan Cai, Ning Zhang, Xiaoming Tao, and Yang Chai**

Solar-driven overall water splitting based on metal sulfide semiconductor photocatalysts remains as a challenge owing to the strong charge recombination and deficient catalytic active sites. Additionally, significant inhibition of back reactions, especially the oxidation of sulfide ions during the photocatalytic water oxidation catalysis, is an arduous task that requires an efficient photogenerated hole transfer dynamics. Here, a ternary dumbbell-shaped catalyst based on RuO_2/CdS/MoS_2 with spatially separated catalytic sites is developed to achieve simultaneous production of hydrogen and oxygen under simulated solar-light without any sacrificial agents. Particularly, MoS_2 nanosheets anchored on the two ends of CdS nanowires are identified as a reduction cocatalyst to accelerate hydrogen evolution, while RuO_2 nanoparticles as an oxidation cocatalyst are deposited onto the sidewalls of CdS nanowires to facilitate oxygen evolution kinetics. The density functional theory simulations and ultrafast spectroscopic results reveal that photogenerated electrons and holes directionally migrate to MoS_2 and RuO_2 catalytic sites, respectively, thus achieving efficient charge carrier separation. The design of ternary dumbbell structure guarantees metal sulfides against photocorrosion and thus extends their range in solar water splitting.

The global energy demand continues to rise, which presents inextricably serious challenges to environment issues, and drives the quest for clean and renewable energy sources alternative to fossil fuels.[1–3] It has been regarded as a simple and cost-effective method to produce clean hydrogen fuel by photocatalytic overall water splitting,[4–6] comparable to fossil-fuel-derived hydrogen due to its simplicity and low cost.[7–9] However, the photocatalysts for water splitting in previously reported literature still face grand challenges: 1) most of photocatalysts suffer from weak visible light response owing to their large bandgap;[10–12] 2) O_2 evolution from semiconductor photocatalysts is difficult due to multiple electrons and protons transfer process for the formation of O–O bond (1.23 eV).[13–16] In this regard, it is vital to develop narrow-bandgap and low-cost photocatalysts capable of decomposing water into hydrogen and oxygen to maximize the photoconversion efficiency.

Transitional metal chalcogenides is a promising candidate for efficient solar energy harvesting due to their simple chemical composition, narrow bandgap, and appropriate band structure.[17–20] The structure of 1D metal chalcogenides with reduction-cocatalyst tip possesses a few unique advantages in photocatalytic water splitting, such as fully exposed active sites, effective hole localization, and long-distance electron transport.[21–26] For instance, 1D CdS nanorods with Pt nanoparticles (NPs) at the end of nanorods can show impressive photocatalytic H_2 evolution performance with a high quantum efficiency of 9.6% under the light illumination with the wavelength of 455 nm.[27] This optimized reduction-cocatalyst-tipped semiconductor nanostructure fully exploits the benefits of interfacial charge separation between photogenerated electrons transferring to Pt cocatalyst and holes remaining on the CdS nanorods, thus resulting in longer electron lifetime. The improvement of the photogenerated electron lifetime is closely associated with the introduction of sacrificial electron donors. With the absence of sacrificial electron donors, the photoinduced holes accumulated on the sidewalls of 1D metal sulfide tend to oxidize lattice sulfide ions rather than involve in oxygen evolution.[28,29] Consequently, an efficient hole transfer is a key step to achieve high-efficiency solar-to-fuel conversion.

Recently, researchers employed metal-based molecular cocatalysts as holes collector and investigated the effect of tunable ligand structure on water oxidation activity.[30,31] Nevertheless, the metal-based molecular cocatalysts require complicated organic synthetic process and exhibit poor stability as a result of hole-induced ligand oxidation.[32,33] Compared with metal-based molecular cocatalysts, non-photoresponsive metal oxides, such as

Dr. B. Qiu, Dr. L. Cai, Dr. N. Zhang, Prof. Y. Chai
Department of Applied Physics
The Hong Kong Polytechnic University
Hung Hom, Kowloon, Hong Kong 999077, P. R. China
E-mail: ychai@polyu.edu.hk
Dr. B. Qiu, Dr. L. Cai, Dr. N. Zhang, Prof. Y. Chai
The Hong Kong Polytechnic University Shenzhen Research Institute
Shenzhen 518057, P. R. China
Prof. X. Tao
Institute of Textiles and Clothing
The Hong Kong Polytechnic University
Hung Hom Kowloon, Hong Kong 999077, P. R. China
The ORCID identification number(s) for the author(s) of this article can be found under https://doi.org/10.1002/advs.201903568

DOI: 10.1002/advs.201903568

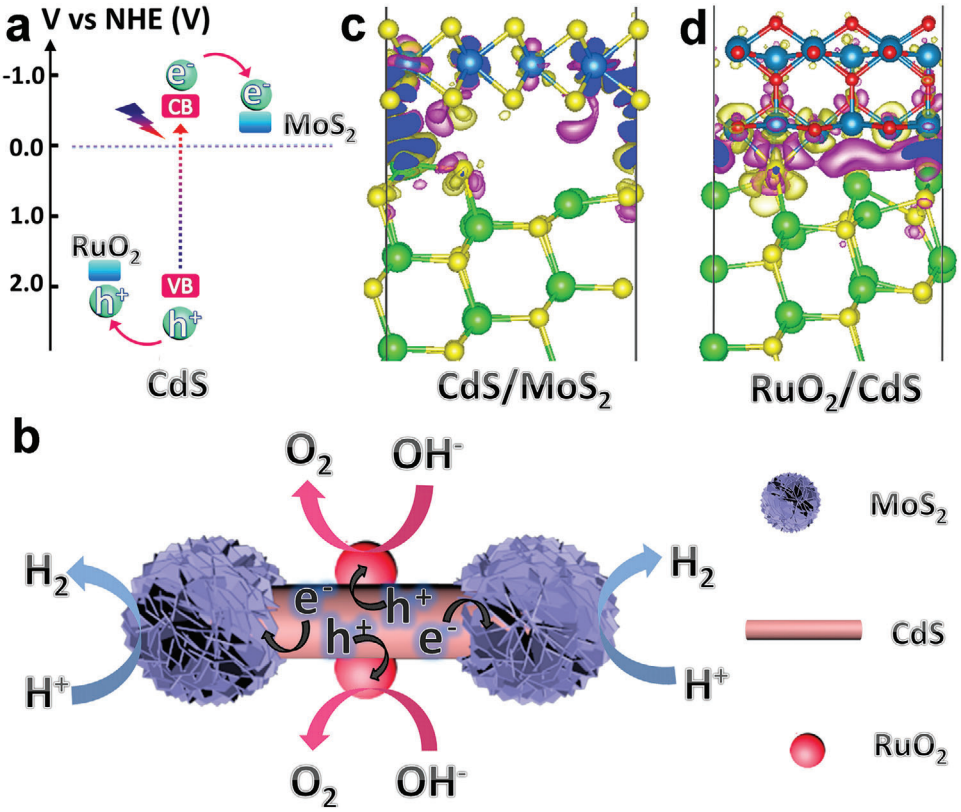

Figure 1. a) The feasibility analysis of solar-driven overall water splitting on CdS photocatalysts decorated with reduction (MoS_2) and oxidation (RuO_2) cocatalysts. b) The migration path of photogenerated electrons and holes in photocatalytic water-splitting reaction driven by RuO_2/CdS/MoS_2 nanodumbbells. Differential charge density [$\Delta\rho = \rho$(A/CdS) − ρ(A) − ρ(CdS) (A = MoS_2 or RuO_2)] of c) CdS/MoS_2 and d) RuO_2/CdS, respectively. Electron excess and deficiency were displayed as purple and light yellow isosurfaces, respectively, with the level of 0.003 e Å^{-3}.

RuO_2 and IrO_2, are alternative oxidation cocatalysts with low resistivity and high corrosion resistance.[34–36] Therefore, we can expect that the deposition of metal oxides cocatalysts onto the sidewalls of 1D metal sulfide structure can effectively transfer multiple holes from sulfide to oxidation cocatalysts sites, which is indispensable for water oxidation.

In this work, we design and fabricate a nanodumbbell structure photocatalyst based on CdS nanowires anchored with MoS_2 (electron collector) and RuO_2 (hole collector) dual cocatalysts to successfully achieve simultaneous H_2 and O_2 evolution (**Figure 1**a). MoS_2 NSs as electron trappers are decorated at the both tips of CdS nanowires, while RuO_2 NPs as hole collectors are deposited on the sidewalls of CdS nanowires. The photogenerated electrons and holes on the CdS nanowires flow to tips and sidewalls, respectively, and charges accumulated on the corresponding cocatalysts subsequently take part in overall water splitting (Figure 1b).

The band structure of CdS nanowires was first investigated to analyze the possibility of photocatalytic overall water splitting (Figure S1, Supporting Information). The bandgap of CdS is determined to be 2.12 eV from the Tauc plot (Figure S1a,b, Supporting Information), and its valence band (VB) potential is calculated to be 1.88 eV from X-ray photoelectron spectroscopy (XPS) (Figure S1c, Supporting Information). The conduction band (CB) position is thus estimated at −0.24 eV. Electronic band structure of CdS (Figure S1d, Supporting Information) further shows that the reduction level for H_2 is positioned below the CB of CdS, while the oxidation level for H_2O to H_2O_2 or O_2 is above the VB of CdS, which suggests thermodynamical possibility for photocatalytic overall water splitting.[37] After introducing dual cocatalysts onto CdS nanowires, we hypothesize that electron coupling effects are existed at both CdS/MoS_2 and CdS/RuO_2 interfaces, which is essential for photogenerated electrons and holes transfer. We performed density function theory (DFT) simulations to investigate the coupling effect and charge transfer route at the interfaces. These two heterostructures based on CdS/MoS_2 and RuO_2/CdS are formed by the strong chemical bonding interactions, due to the high binding energies of −0.30 and −1.08 J m^{-2}, respectively. Furthermore, Figure 1c,d shows high differential charge density at the CdS/MoS_2 and RuO_2/CdS junction region, indicating the remarkable charge transfer occurs at the interfaces. Clearly, the outmost Cd atoms of CdS donate electrons to the S atoms of MoS_2 at the MoS_2/CdS heterostructure interface (Figure 1c). Bader charge analysis further indicates 0.82 electrons transfer from CdS to MoS_2. For the RuO_2/CdS system (Figure 1d), a significant reconstruction of interfacial atoms from CdS is caused by the polarization effect of RuO_2, resulting in more complicated electrons redistribution at the interface of RuO_2/CdS. The charge transfer (0.62 electrons) calculated from Bader charge reveals the formation of positively charged RuO_2 and negatively charged CdS at the RuO_2/CdS interface, indicating the surface of RuO_2 attracts holes from the adjacent CdS. Our

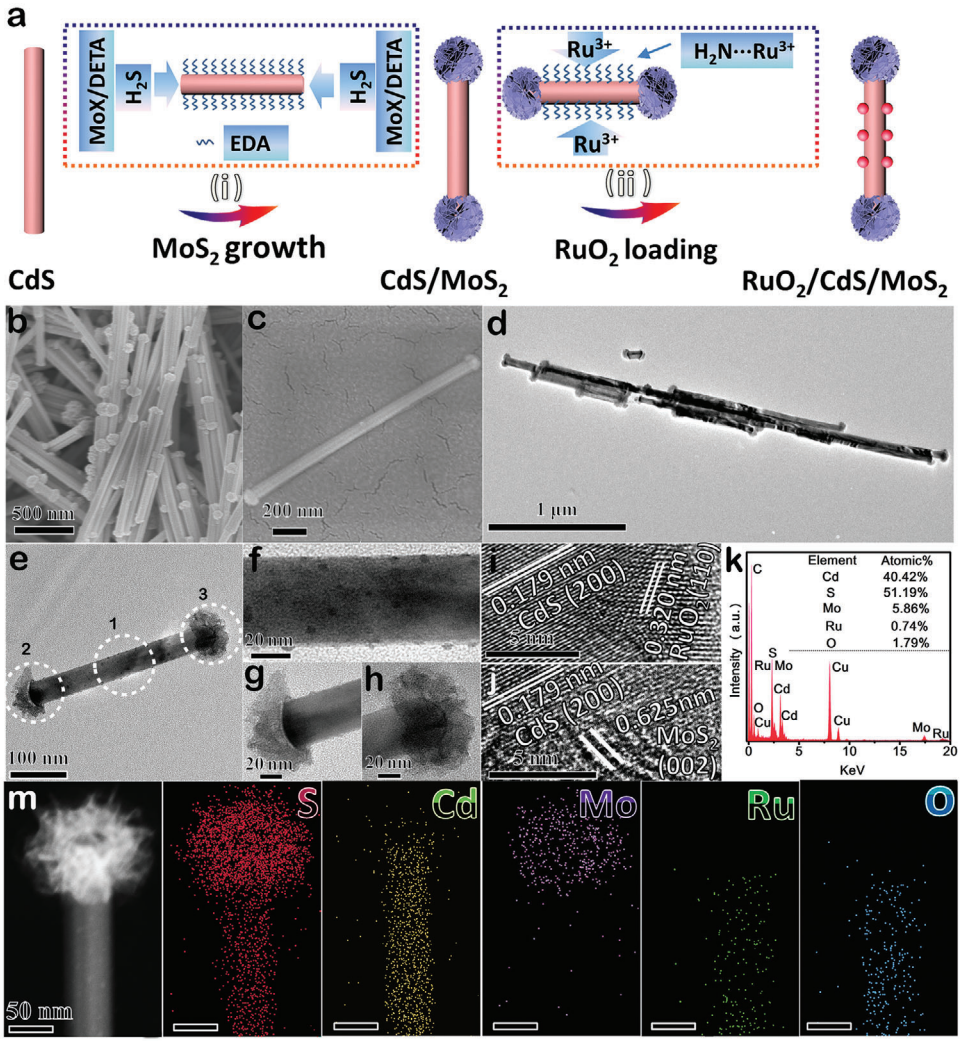

Figure 2. a) Schematic illustration of RuO_2/CdS/MoS_2 nanodumbbell preparation process (i: selective growth of MoS_2 NSs at the two ends of CdS nanowires; ii: anchoring RuO_2 NPs on the sidewalls of CdS/MoS_2 nanodumbbells). b,c) SEM images and d,e) TEM images of RuO_2/CdS/MoS_2 nanodumbbells. f–h) The corresponding magnified TEM images for selected three part (1,2,3) in (e). i,j) HRTEM images of RuO_2/CdS/MoS_2 nanodumbbells. k) EDX spectrum and m) the corresponding element mapping of S, Cd, Mo, Ru, O.

calculations suggest that the strong interface coupling on both CdS/MoS_2 and RuO_2/CdS enables efficient interfacial charge carrier transfer in ternary RuO_2/CdS/MoS_2 structure, which is essential for high photocatalytic performance.

We designed a synthetic strategy to fabricate the ternary RuO_2/CdS/MoS_2 photocatalyst with nanodumbbells structure (**Figure 2**a). Amine-functionalized CdS nanowires with average diameter of 60–70 nm were first prepared through a solvothermal approach by using ethanediamine as the chelating agent, as confirmed by scanning electron microscope (SEM) (Figure S2a,b, Supporting Information) and transmission electron microscope (TEM) images (Figure S2c,d, Supporting Information). X-ray diffraction (XRD) pattern shows characteristic peaks of CdS with hexagonal Wurtzite crystal structure (Figure S3, Supporting Information). The MoS_2 NSs were further decorated with the two ends of amine-functionalized CdS nanowires (CdS/MoS_2) by hydrothermal treatment with Na_2MoO_4 and thioacetamide as the MoS_2 precursors in the mixture of H_2O and diethylenetriamine. The SEM and TEM images (Figure S4, Supporting Information) show that MoS_2 NSs are selectively and symmetrically grown on the two tips of CdS nanowire to form a well-defined nanodumbbell structure. After MoS_2 NSs affixed CdS nanowire tips, the surface-modified $-NH_2$ groups still remain at the sidewalls of CdS nanowires, which is confirmed by Fourier transform infrared spectra (Figure S5, Supporting Information). The strong coordination between Ru^{3+} and $-NH_2$ groups ensures that the dispersion of Ru^{3+} ions on the sides of CdS/MoS_2.[38] Following a thermal treatment process, RuO_2 NPs were selectively formed on the sidewalls of CdS nanowires. The morphology characterizations manifest that the prepared RuO_2/CdS/MoS_2 sample still maintains symmetrical tip-coated structure (Figure 2b,c), and some ultrasmall RuO_2 NPs are precisely located on the sidewalls of CdS nanowires (Figure 2d,e). More closer TEM observations (Figure 2f,g,h) on the three selected regions (Figure 2e) and their corresponding energy dispersive X-ray (EDX) spectra (Figure S6, Supporting Information) show that the RuO_2 NPs with

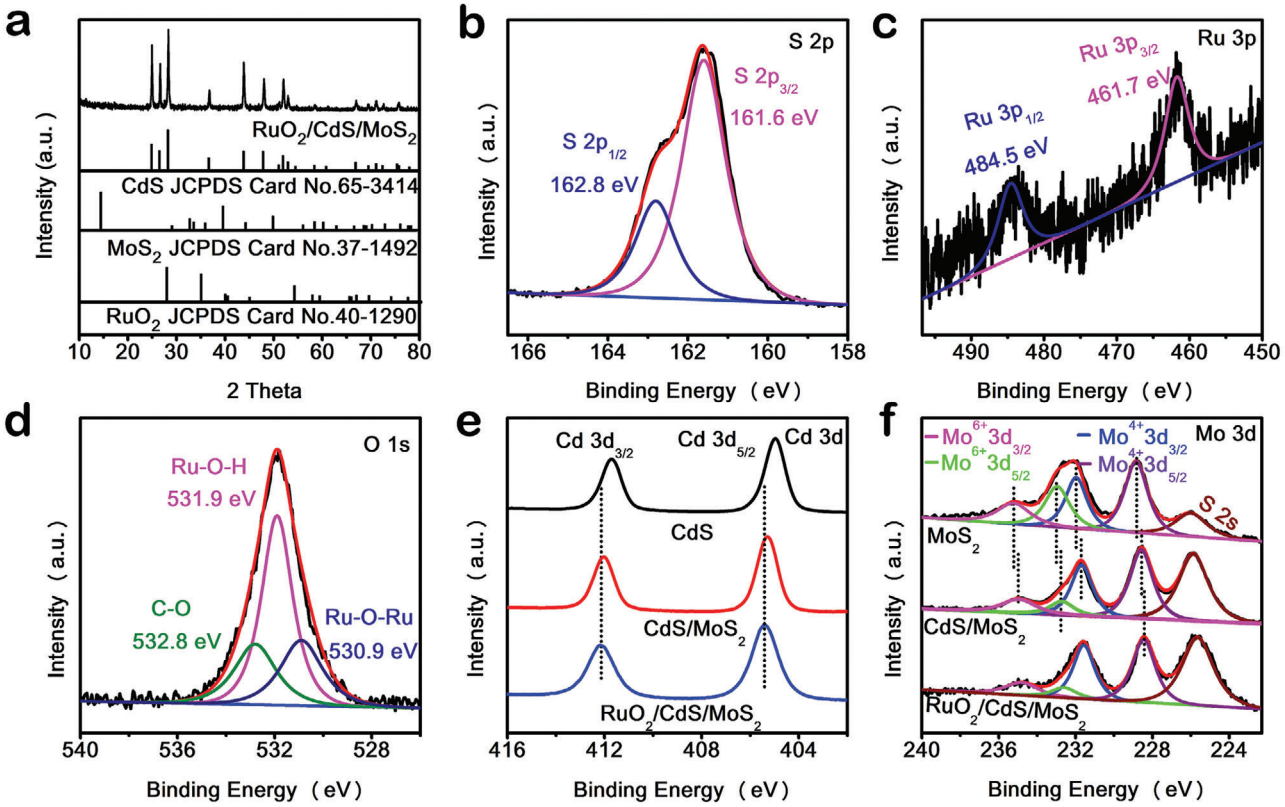

Figure 3. a) XRD pattern of $RuO_2/CdS/MoS_2$ nanodumbbells. High resolution XPS spectra of S 2p b), Ru 3p c), and O 2p d) of $RuO_2/CdS/MoS_2$ nanodumbbells. e) High-resolution Cd 3d XPS spectra of CdS, CdS/MoS_2, and $RuO_2/CdS/MoS_2$. f) High-resolution Mo 3d XPS spectra of MoS_2, CdS/MoS_2, and $RuO_2/CdS/MoS_2$.

average size of 4 nm are selectively loaded on the sidewalls of CdS rather than the MoS_2 tips. A high resolution TEM (HRTEM) image of the sidewall of $RuO_2/CdS/MoS_2$ (Figure 2i) reveals that two sets of lattice distances of 0.179, and 0.320 nm, assigning to (200) plane of CdS and (110) planes of RuO_2, respectively. As for the end of $RuO_2/CdS/MoS_2$ (Figure 2j), the interplanar spacings of 0.179 and 0.625 nm are ascribed to (200) plane of CdS and (002) plane of MoS_2, respectively. The spatially separated distribution of MoS_2 and RuO_2 on CdS is further confirmed by high-angle annular dark-field scanning transmission electron microscopy and elemental mapping. As displayed in Figure 2k,m, MoS_2 NSs and RuO_2 NPs are preferentially formed at the tips and sidewalls of CdS nanowires, respectively. For comparison, RuO_2/CdS nanowires were also synthesized by depositing RuO_2 onto the sidewalls of CdS nanowires, as confirmed by SEM, TEM, and XRD pattern (Figure S7, Supporting Information).

The crystal structure and element composition of $RuO_2/CdS/MoS_2$ are confirmed by XRD patterns and XPS spectra. The XRD pattern (**Figure 3**a) indicates that as-prepared sample still preserves hexagonal Wurtzite-structured phase CdS (JCPDS No. 65-3414), and no characteristic peaks of MoS_2 or RuO_2 are observed due to their relative low Mo (9.31 wt%) and Ru (0.96 wt%) concentration, which is confirmed by the inductively coupled plasma mass spectrometry (ICP-MS) (Table S1, Supporting Information). XPS survey spectrum (Figure S8, Supporting Information) shows the coexistence of Cd, S, Mo, Ru, and O elements, indicating successful deposition of MoS_2 and RuO_2 on CdS. The high resolution XPS signal (Figure 3b) of S 2p can be well deconvoluted into two separate peaks located at 162.8 and 161.6 eV, corresponding to S $2p_{1/2}$ and S $2p_{3/2}$ in the form of S^{2-}, respectively.[39,40] The high resolution Ru 3p XPS spectrum (Figure 3c) exhibits the doublets for Ru $3p_{1/2}$ and Ru $3p_{3/2}$ peaks at 484.5 and 461.7 eV, respectively, as expected for RuO_2.[41] With regard to the XPS spectrum of O 1s (Figure 3d), two discrete peaks at 530.9 and 531.9 eV are indexed to Ru–O–Ru and Ru–O–H, and the other one at 532.8 eV is attributed to C–O bond, which originates from the surface oxygenated groups.[42,43]

To achieve fast interfacial charge transfer at the heterostructure interface, the formation of intimate electron coupling interface is of great importance. Compared to those of CdS, Cd 3d peaks for CdS/RuO_2 demonstrate negative shift of 0.1 eV (Figure S9a, Supporting Information), suggesting more free electrons accumulation at CdS caused by the holes transfer from CdS to RuO_2 after their combination, which is in agreement with the DFT simulation results. Similarly, the S 2p peaks for CdS/RuO_2 also display negative shift in binding energy (Figure S9b, Supporting Information). However, an obvious shift of 0.3 eV to high binding energy region can be also observed in Cd 3d XPS spectrum of CdS/MoS_2 as compared to that of CdS (Figure 3e), unraveling electron transfer from CdS to MoS_2.[44] Moreover, a slight shift of 0.1 eV toward the high binding energy is observed after further RuO_2 loading, suggesting a strong electron coupling effect

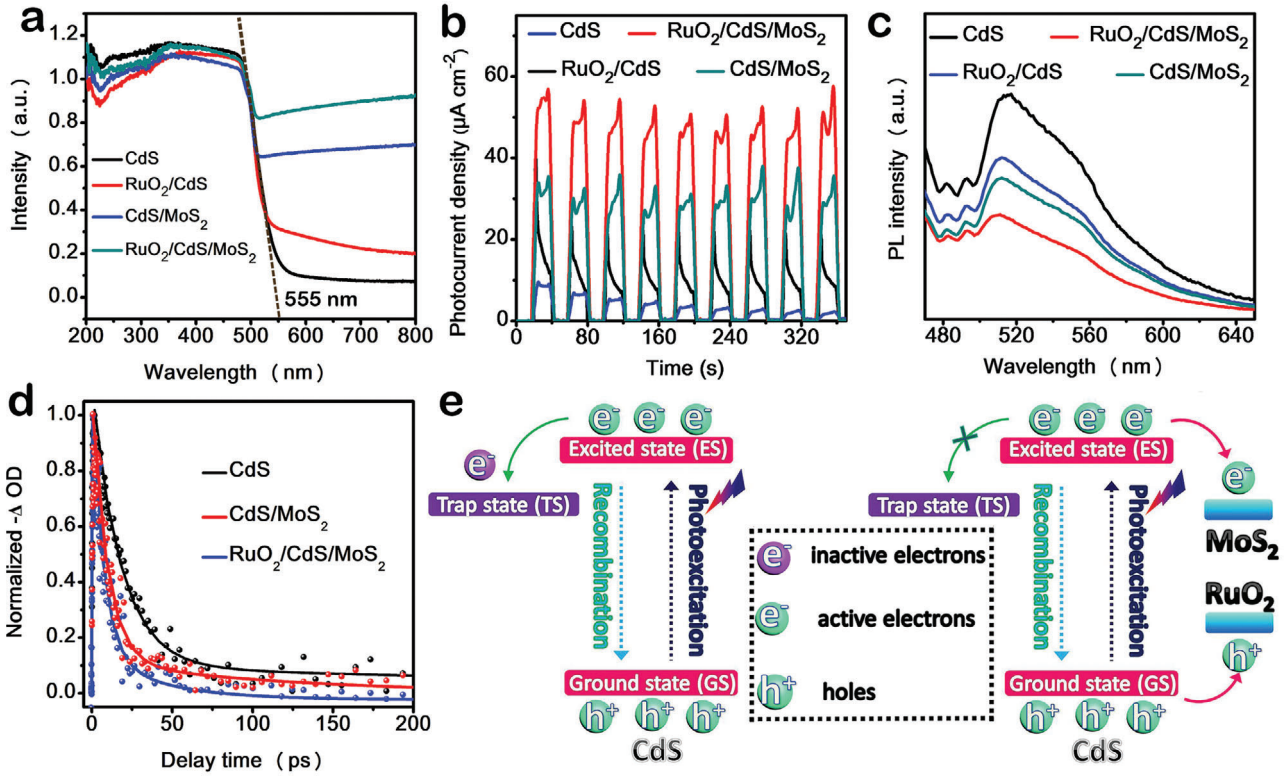

Figure 4. a) UV–vis diffuse reflectance spectra, b) Transient photocurrents, and c) PL spectra of CdS, RuO_2/CdS, CdS/MoS_2, and RuO_2/CdS/MoS_2. d) Normalized fs-TA decay kinetics (dotted line) with a biexponential function fitting curves (solid lines). e) Schematic representation of proposed charge transfer and recombination routes in CdS and RuO_2/CdS/MoS_2.

between CdS and RuO_2, which contributes to the charge transfer from CdS to RuO_2. Meanwhile, Mo 3d peaks for MoS_2 show continuous shift toward low binding energy after hybridization with MoS_2 and RuO_2 in turn (Figure 3f).

Ultraviolet visible (UV–vis) diffuse reflectance spectra were employed to investigate the light harvesting capability of the as-prepared samples. As displayed in **Figure 4**a, the light absorption of CdS/MoS_2 nanodumbbells is clearly increased in the visible light region as compared to CdS nanowires, which is attributed to the black color of MoS_2.[45] After further RuO_2 NPs depositing, a stronger light response can be observed for RuO_2/CdS/MoS_2. It is also noted that negligible shift in absorption edge of RuO_2/CdS/MoS_2 can be observed, which manifests that Ru, O, or Mo atom is undoped into the crystal lattice of CdS. The charge separation and transfer behavior of the as-made samples were studied by transient photocurrent response spectroscopy, electrochemical impedance spectra (EIS), and photoluminescence (PL) spectroscopy. As displayed in Figure 4b, RuO_2/CdS/MoS_2 shows the highest photocurrent intensity, suggesting enhancement of charge separation efficiency by introducing spatially separated MoS_2 and RuO_2 dual cocatalysts. Furthermore, the EIS spectra (Figure S10, Supporting Information) demonstrate that the semicircle diameter of RuO_2/CdS/MoS_2 is the smallest one among all the samples, indicating the optimal interfacial charge-carrier transfer ability on the surface of RuO_2/CdS/MoS_2. In addition, PL quenching experiments were conducted to investigate the electron transfer dynamics. The most significant quenching of PL is observed by the decoration of dual cocatalysts, testifying the prolonged lifetime of photogenerated charge carrier in RuO_2/CdS/MoS_2. To better understand the spatial separation behavior of photoinduced charge carriers in RuO_2/CdS/MoS_2, two photodeposition reactions, reduction of Au^{3+} with lactic acid as hole collectors and oxidation of Mn^{2+} with IO_3^- as electron acceptors were carried out, respectively. As indicated in Figure S11 (Supporting Information), Au NPs were selectively loaded on the MoS_2 tips, suggesting that the photogenerated electrons tend to migrate to MoS_2 sites for reduction reaction. By contrast, MnO_x NSs derived from Mn^{2+} oxidation were deposited only on RuO_2 part (Figure S12, Supporting Information), revealing the photogenerated holes are inclined to accumulate on RuO_2 sites for oxidation reaction.

To further ascertain the nature of the photoinduced charge carrier transfer interaction, femtosecond transient absorption (Fs-TA) spectroscopy was carried out by employing pump–probe technique using 400 nm laser as a pump pulse and a white light continuum of 440–700 nm as the probe pulse. Upon 400 nm excitation, these three samples of CdS, CdS/MoS_2, and RuO_2/CdS/MoS_2 show the distinctly negative absorption peak at 475 nm (Figure S13, Supporting Information), which is attributed to photobleaching of the ground state (GS) absorption.[46] Transient absorption (TA) kinetic decay traces of the three samples are fitted with biexponential decay, and the fitting parameters are summarized in Table S2 (Supporting Information). Upon light irradiation, photoinduced electrons can be

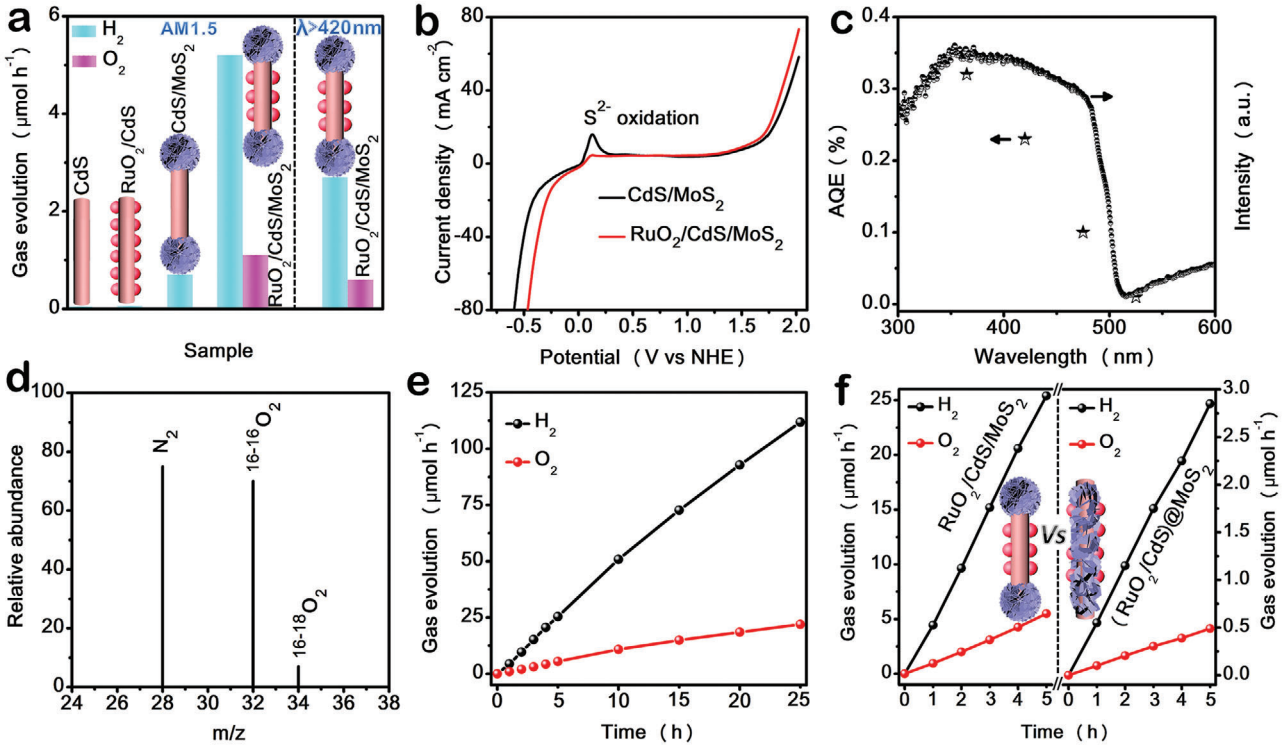

Figure 5. a) Gases evolution rate from water under the irradiation of a 300 W Xe lamp (AM1.5 air mass filter) catalyzed by CdS, RuO_2/CdS, CdS/MoS_2, and RuO_2/CdS/MoS_2, and gases evolution rate from water under the irradiation of visible light (λ >420 nm) catalyzed by RuO_2/CdS/MoS_2. b) LSV curves of CdS and RuO_2/CdS/MoS_2 in 1 M KOH electrolyte with a scanning rate of 50 mV s^{-1}. c) AQE as a function of the irradiation wavelength in overall water-splitting reaction over RuO_2/CdS/MoS_2. d) GC-MS signals of the gas generated over RuO_2/CdS/MoS_2 for photocatalytic splitting of water containing 20% $H_2{}^{18}O$. e) The durable experiment of RuO_2/CdS/MoS_2. f) Time course of hydrogen and oxygen evolution under the irradiation of a 300 W Xe lamp (AM1.5 air mass filter) catalyzed by (RuO_2/CdS)@MoS_2 and RuO_2/CdS/MoS_2.

first excited from GS to excited state (ES) followed by two fast processes involving charge recombination from ES to GS and charges trapping from ES to inactive trap states (TS). It is noted that the electrons on TS are inactive and not involved into photocatalytic reaction.[47] For CdS nanowires, the decay observed within 10 ps (τ_1, Table S2, Supporting Information) is assigned to the active charge recombination from ES to GS, while the lifetime of 350.8 ps (τ_2, Table S2, Supporting Information) is attributed to the charge transfer process from ES to TS. Regarding CdS/MoS_2, the fast decay component of 8.1 ps (τ_1, Table S2, Supporting Information) is mainly ascribed to the charge recombination from ES to GS in CdS. The lifetime of 123.5 ps (τ_2, Table S2, Supporting Information) is attributed to the charge transfer from ES of CdS to MoS_2 rather than from ES to TS in CdS, because the efficient electron capture ability of MoS_2 prevents photogenerated electrons from trapping into inactive TS in CdS. After the decoration of RuO_2 on the sidewalls of CdS/MoS_2 nanodumbbells, the lifetime (τ_2, Table S2, Supporting Information) is further reduced to 40.8 ps, revealing that the introduction of RuO_2 promotes electron transfer process from ES of CdS to MoS_2, which accords with the PL results.

The photocatalytic activity of the as-prepared samples were evaluated by hydrogen and oxygen evolution from water-splitting reaction under simulated solar light irradiation (a 300 W Xe lamp equipped with AM1.5 optical filter) without any sacrificial reagents. As indicated in **Figure 5**a, both bare CdS and RuO_2/CdS nanowires show negligible H_2 production activity, while CdS/MoS_2 nanodumbbells display moderate H_2 evolution activity (0.7 μmol h^{-1}) due to the decreased charge recombination rate in terms of the electron transfer from CdS to MoS_2. After further depositing of RuO_2 NPs, the hydrogen evolution rate of RuO_2/CdS/MoS_2 nanodumbbells can be remarkably improved and reach up to 5.2 μmol h^{-1}, and O_2 evolution proceeds continuously at a rate of 1.1 μmol h^{-1}. It should be also noted that RuO_2/CdS/MoS_2 achieves photocatalytic water splitting into H_2 (2.7 μmol h^{-1}) and O_2 (0.6 μmol h^{-1}) under visible light irradiation (λ>420 nm), indicating the efficient solar energy harvesting of RuO_2/CdS/MoS_2. Besides, control experiments show that no O_2 evolution was detected by gas chromatography (GC) when CdS/MoS_2 was used as photocatalyst over a 5 h reaction period, which indicates a well-established photocorrosion reaction between S^{2-} and the holes remaining on the sides for CdS/MoS_2 nanodumbbells. The TEM observations (Figure S14a, Supporting Information) and XRD patterns (Figure S14b, Supporting Information) of CdS/MoS_2 after the water-splitting reaction further prove that photoinduced holes can readily oxidize the lattice S^{2-} ions of CdS.[48] Similar phenomenon is also observed for bare CdS nanowires (Figure S14c,d, Supporting Information). Furthermore, the linear sweep voltammetry (LSV) curve of the RuO_2/CdS/MoS_2 nanodumbbells demonstrates an obvious reduction of the S^{2-} ions oxidation peak along with the decreased overpotential of oxygen evolution as compared to that of

the CdS/MoS_2 nanodumbbells (Figure 5b), indicating the holes transfer from CdS to RuO_2 in $RuO_2/CdS/MoS_2$ and the minimization of S^{2-} ions oxidation during water oxidation. Besides, the dependence of photocatalytic performance on the loading amounts of MoS_2 and RuO_2 was illustrated in Figure S15 (Supporting Information). It can be observed that the nominal loading amounts of MoS_2 and RuO_2 were 15.52 and 1.26 wt%, respectively (the loading amounts of MoS_2 and RuO_2 are calculated from the ICP results of Mo and Ru, respectively).

Although simultaneous H_2 and O_2 evolution based on $RuO_2/CdS/MoS_2$ nanodumbbells is achieved, the H_2/O_2 ratio deviated from the stoichiometric value of 2. To unravel the intrinsic reason, we used an iodometric method to detect potentially produced H_2O_2. As expected, with the water-splitting proceeding, a trace amount of H_2O_2 was observed, and the concentration of H_2O_2 gradually increased over 5 h (Figure S16, Supporting Information), suggesting part of holes on the RuO_2 sites take part in H_2O_2 evolution via 2-eletrons pathway, which is supported by energy band structure (Figure S1d, Supporting Information). To further confirm that the detected O_2 was indeed generated from H_2O splitting, an isotopes labeling experiment was performed in a mixture of H_2O and $H_2{}^{18}O$. As shown in Figure 5d, a signal at m/z = 34 is identified as $^{16-18}O_2$, verifying that O_2 is formed from photocatalytic overall water splitting.[49] In addition, the stability experiment demonstrates negligible deterioration of photocatalytic activity for $RuO_2/CdS/MoS_2$ during 25 h irradiation (Figure 5e). SEM and TEM observations (Figure S17a–e, Supporting Information) show the recovered sample still retain the dumbbell morphology without obvious photocorrosion. The elemental composition and crystal structure remain unchanged, as confirmed by element mapping (Figure S17f, Supporting Information) and XRD pattern (Figure S18, Supporting Information), indicating the excellent stability of $RuO_2/CdS/MoS_2$. The apparent quantum efficiency (AQE) for $RuO_2/CdS/MoS_2$ during overall water splitting as a function of the incident light wavelength was displayed in Figure 5c. The AQE values for $RuO_2/CdS/MoS_2$ reach 0.32% at 365 nm, 0.23% at 425 nm, and 0.10% at 475 nm. When the light absorption at wavelengths is longer than 500 nm, the AQE value is nearly zero due to the low absorption efficiency for CdS in the visible-light region beyond 500 nm.

To highlight the advantages of nanodumbbell structure with spatial separated sites in photocatalysis, we prepared $(RuO_2/CdS)@MoS_2$ core–shell photocatalyst with randomly loaded catalytic sites as control sample. As shown in Figure S19a (Supporting Information), RuO_2 NPs are first deposited on the sidewalls of CdS nanowires and subsequently the obtained RuO_2/CdS nanowires are wrapped by MoS_2 NSs to form $(RuO_2/CdS)@MoS_2$ core–shell structure. SEM images (Figure S19b,c, Supporting Information), TEM images (Figure S19d–f, Supporting Information), and element mapping (Figure S19g,h, Supporting Information) indicate the successful preparation of $(RuO_2/CdS)@MoS_2$ core–shell structure. Besides, there are no distinct differences in light absorption (Figure S20a, Supporting Information), crystal structure (Figure S20b, Supporting Information), and the loading amount of dual cocatalysts (Table S2, Supporting Information) between $(RuO_2/CdS)@MoS_2$ and $RuO_2/CdS/MoS_2$, eliminating the effects of these three factors on photocatalytic performance. As indicated in Figure 5f, the rate of gas evolution for $(RuO_2/CdS)@MoS_2$ are almost 10 times faster than that of $(RuO_2/CdS)@MoS_2$ (0.57 μmol h^{-1} H_2 and 0.1 μmol h^{-1} O_2). The origin of the remarkably enhanced performance is attributed to the spatially separated catalytic sites for the H_2 and O_2 evolution. Basically, for $RuO_2/CdS/MoS_2$ dumbbell structure, the photogenerated electrons and holes have a remarkably tendency to locate at MoS_2 and RuO_2, respectively, thus facilitating charge separation. Nevertheless, regarding $(RuO_2/CdS)@MoS_2$, there are lots of contact interface between MoS_2 and RuO_2 due to their random loading (Figure S21, Supporting Information), which leads to the recombination of photoinduced charge carriers at the interfaces.

In conclusion, we demonstrated that a ternary $RuO_2/CdS/MoS_2$ photocatalyst with well-defined dumbbell structure evolved H_2 and O_2 via a water-splitting reaction under simulated solar light irradiation. The construction of spatially separated dual cocatalysts on CdS nanowires enables the photoexcited electrons and holes to transfer expeditiously from CdS to the MoS_2 and RuO_2 catalytic sites, respectively, resulting in a superior and durable photocatalytic water-splitting activity. This work provides an efficient strategy for the design of metal-sulfide-based photocatalysts with high overall water-splitting performance.

Supporting Information

Supporting Information is available from the Wiley Online Library or from the author.

Acknowledgements

This work was supported by the Science, Technology and Innovation Commission of Shenzhen (No. JCYJ20180507183424383), the Research Grant Council of Hong Kong (No. PolyU 152145/15E), and the Hong Kong Polytechnic University (G-YW2A).

Conflict of Interest

The authors declare no conflict of interest.

Keywords

charge transfer, dual cocatalysts, nanodumbbells, overall water splitting, spatially separated sites

Received: December 11, 2019
Revised: April 12, 2020
Published online: July 14, 2020

[1] X. Chen, S. Shen, L. Guo, S. S. Mao, *Chem. Rev.* **2010**, *110*, 6503.
[2] N. S. Lewis, *Science* **2016**, *351*, aad1920.
[3] Y. Hu, F. Zhan, Q. Wang, Y. Sun, C. Yu, X. Zhao, H. Wang, R. Long, G. Zhang, C. Gao, W. Zhang, J. Jiang, Y. Tao, Y. Xiong, *J. Am. Chem. Soc.* **2020**, *142*, 5618.
[4] Z. Wang, Y. Inoue, T. Hisatomi, R. Ishikawa, Q. Wang, T. Takata, S. Chen, N. Shibata, Y. Ikuhara, K. Domen, *Nat. Catal.* **2018**, *1*, 756.

[5] H. Dotan, A. Landman, S. W. Sheehan, K. D. Malviya, G. E. Shter, D. A. Grave, Z. Arzi, N. Yehudai, M. Halabi, N. Gal, N. Hadari, C. Cohen, A. Rothschild, G. S. Grader, *Nat. Energy* **2019**, *4*, 786.
[6] T. T. Zhuang, Y. Liu, Y. Li, Y. Zhao, L. Wu, J. Jiang, S. H. Yu, *Angew. Chem., Int. Ed.* **2016**, *55*, 6396.
[7] Q. Wang, M. Nakabayashi, T. Hisatomi, S. Sun, S. Akiyama, Z. Wang, Z. Pan, X. Xiao, T. Watanabe, T. Yamada, N. Shibata, T. Takata, K. Domen, *Nat. Mater.* **2019**, *18*, 827.
[8] B. Qiu, M. Xing, J. Zhang, *Chem. Soc. Rev.* **2018**, *47*, 2165.
[9] M. Wang, Y. Zuo, J. Wang, Y. Wang, X. Shen, B. Qiu, L. Cai, F. Zhou, S. P. Lau, Y. Chai, *Adv. Energy Mater.* **2019**, *9*, 1901801.
[10] B. Qiu, Y. Deng, Q. Li, B. Shen, M. Xing, J. Zhang, *J. Phys. Chem. C* **2016**, *120*, 12125.
[11] C. Gao, J. Wang, H. Xu, Y. Xiong, *Chem. Soc. Rev.* **2017**, *46*, 2799.
[12] Q. Zhu, B. Qiu, M. Du, M. Xing, J. Zhang, *Ind. Eng. Chem. Res.* **2018**, *57*, 8125.
[13] B. Qiu, C. Wang, N. Zhang, L. Cai, Y. Xiong, Y. Chai, *ACS Catal.* **2019**, *9*, 6484.
[14] J. Liu, Y. Liu, N. Liu, Y. Han, X. Zhang, H. Huang, Y. Lifshitz, S.-T. Lee, J. Zhong, Z. Kang, *Science* **2015**, *347*, 970.
[15] K. Iwashina, A. Iwase, Y. H. Ng, R. Amal, A. Kudo, *J. Am. Chem. Soc.* **2015**, *137*, 604.
[16] B. Qiu, L. Cai, Y. Wang, S. Ma, Y. H. Tsang, Y. Chai, *Mater. Today Energy* **2019**, *11*, 89.
[17] K. Li, M. Han, R. Chen, S. L. Li, S. L. Xie, C. Mao, X. Bu, X. L. Cao, L. Z. Dong, P. Feng, *Adv. Mater.* **2016**, *28*, 8906.
[18] J. Chen, X. J. Wu, L. Yin, B. Li, X. Hong, Z. Fan, B. Chen, C. Xue, H. Zhang, *Angew. Chem., Int. Ed.* **2015**, *54*, 1210.
[19] L. Ma, S. Liang, X. L. Liu, D. J. Yang, L. Zhou, Q. Q. Wang, *Adv. Funct. Mater.* **2015**, *25*, 898.
[20] B. Qiu, Q. Zhu, M. Xing, J. Zhang, *Chem. Commun.* **2017**, *53*, 897.
[21] K. Zhang, J. K. Kim, M. Ma, S. Y. Yim, C. L. Lee, H. Shin, J. H. Park, *Adv. Funct. Mater.* **2016**, *26*, 4527.
[22] J. U. Bang, S. J. Lee, J. S. Jang, W. Choi, H. Song, *J. Phys. Chem. Lett.* **2012**, *3*, 3781.
[23] J. Y. Choi, D. Jeong, S. J. Lee, D.-g. Kang, S. K. Kim, K. M. Nam, H. Song, *Nano Lett.* **2017**, *17*, 5688.
[24] N. Waiskopf, Y. Ben-Shahar, U. Banin, *Adv. Mater.* **2018**, *30*, 1706697.
[25] P. Zhang, L. Yu, X. W. Lou, *Angew. Chem., Int. Ed.* **2018**, *57*, 15076.
[26] R. Jiang, B. Li, C. Fang, J. Wang, *Adv. Mater.* **2014**, *26*, 5274.
[27] K. Wu, Z. Chen, H. Lv, H. Zhu, C. L. Hill, T. Lian, *J. Am. Chem. Soc.* **2014**, *136*, 7708.
[28] B. Tian, W. Gao, X. Zhang, Y. Wu, G. Lu, *Appl. Catal., B* **2018**, *221*, 618.
[29] J. Chu, G. Sun, X. Han, X. Chen, J. Wang, W. Hu, I. Waluyo, A. Hunt, Y. Du, B. Song, P. Xu, *Nanoscale* **2019**, *11*, 15633.
[30] H.-W. Tseng, M. B. Wilker, N. H. Damrauer, G. Dukovic, *J. Am. Chem. Soc.* **2013**, *135*, 3383.
[31] O. M. Pearce, J. S. Duncan, N. H. Damrauer, G. Dukovic, *J. Phys. Chem. C* **2018**, *122*, 17559.
[32] C. M. Wolff, P. D. Frischmann, M. Schulze, B. J. Bohn, R. Wein, P. Livadas, M. T. Carlson, F. Jäckel, J. Feldmann, F. Würthner, *Nat. Energy* **2018**, *3*, 862.
[33] S. Ye, C. Ding, M. Liu, A. Wang, Q. Huang, C. Li, *Adv. Mater.* **2019**, *31*, 1902069.
[34] K. Kalyanasundaram, E. Borgarello, D. Duonghong, M. Grätzel, *Angew. Chem. Int. Ed.* **1981**, *20*, 987.
[35] G. Ma, S. Chen, Y. Kuang, S. Akiyama, T. Hisatomi, M. Nakabayashi, N. Shibata, M. Katayama, T. Minegishi, K. Domen, *J. Phys. Chem. Lett.* **2016**, *7*, 3892.
[36] J. Lu, L. Cai, N. Zhang, B. Qiu, Y. Chai, *ACS Appl. Mater. Interfaces* **2019**, *11*, 44214.
[37] Z. Wang, C. Li, K. Domen, *Chem. Soc. Rev.* **2019**, *48*, 2109.
[38] X. Wang, W. Chen, L. Zhang, T. Yao, W. Liu, Y. Lin, H. Ju, J. Dong, L. Zheng, W. Yan, *J. Am. Chem. Soc.* **2017**, *139*, 9419.
[39] B. Qiu, Q. Zhu, M. Du, L. Fan, M. Xing, J. Zhang, *Angew. Chem., Int. Ed.* **2017**, *56*, 2684.
[40] B. Qiu, L. Cai, Y. Wang, X. Guo, S. Ma, Y. Zhu, Y. H. Tsang, Z. Zheng, R. Zheng, Y. Chai, *Small* **2019**, *15*, 1904507.
[41] Z. J. Han, S. Pineda, A. T. Murdock, D. H. Seo, K. K. Ostrikov, A. Bendavid, *J. Mater. Chem. A* **2017**, *5*, 17293.
[42] R. Ge, L. Li, J. Su, Y. Lin, Z. Tian, L. Chen, *Adv. Energy Mater.* **2019**, *9*, 1901313.
[43] H.-S. Park, J. Yang, M. K. Cho, Y. Lee, S. Cho, S.-D. Yim, B.-S. Kim, J. H. Jang, H.-K. Song, *Nano Energy* **2019**, *55*, 49.
[44] J. Ran, B. Zhu, S. Z. Qiao, *Angew. Chem., Int. Ed.* **2017**, *56*, 10373.
[45] J. Ran, G. Gao, F.-T. Li, T.-Y. Ma, A. Du, S.-Z. Qiao, *Nat. Commun.* **2017**, *8*, 13907.
[46] L. Jing, R. Zhu, D. L. Phillips, J. C. Yu, *Adv. Funct. Mater.* **2017**, *27*, 1703484.
[47] R. Godin, Y. Wang, M. A. Zwijnenburg, J. Tang, J. R. Durrant, *J. Am. Chem. Soc.* **2017**, *139*, 5216.
[48] M. Wang, L. Cai, Y. Wang, F. Zhou, K. Xu, X. Tao, Y. Chai, *J. Am. Chem. Soc.* **2017**, *139*, 4144.
[49] L. Liao, Q. Zhang, Z. Su, Z. Zhao, Y. Wang, Y. Li, X. Lu, D. Wei, G. Feng, Q. Yu, *Nat. Nanotechnol.* **2014**, *9*, 69.

